Published in final edited form as:
Biomaterials. 2019 June ; 206: 13–24. doi:10.1016/j.biomaterials.2019.03.026.

A lanthanide-peptide-derived bacterium-like nanotheranostic with high tumor-targeting, -imaging and -killing properties

Wangxiao He[a,b,c,1], **Jin Yan**[d,e,1], **Lijuan Wang**[f,1], **Bo Lei**[e], **Peng Hou**[a,*], **Wuyuan Lu**[b,*,*], and **Peter X. Ma**[d,*,*,*]

[a]Key Laboratory for Tumor Precision Medicine of Shaanxi Province and Department of Endocrinology, The First Affiliated Hospital of Xi'an Jiaotong University, Xi'an, 710061, China

[b]Institute of Human Virology and Department of Biochemistry and Molecular Biology, University of Maryland School of Medicine, Baltimore, MD 21201, USA

[c]Center for Translational Medicine, School of Life Science and Biotechnology and Frontier Institute of Science and Technology, Xi'an Jiaotong University, Xi'an, 710049, China

[d]Department of Biologic and Materials Sciences, Department of Biomedical Engineering, Macromolecular Science and Engineering Center, Department of Materials Science and Engineering, University of Michigan, Ann Arbor, MI 48109, USA

[e]Center for Bioengineering and Regenerative Medicine, Frontier Institute of Science and Technology, Xi'an Jiaotong University, Xi'an, 710049, China

[f]Department of Chemistry, School of Science, Xi'an Jiaotong University, Xi'an, 710049, China

Abstract

Nanostructures formed with bioactive peptides offer an exciting prospect in clinical oncology as a novel class of therapeutic agents for human cancers. Despite their therapeutic potential, however, peptide-based nanomedicines are often inefficacious *in vivo* due to low cargo-loading efficiency, poor tumor cell-targeting specificity and limited drug accumulation in tumor tissues. Here, we describe the design, *via* assembly of a p53-activating peptide termed PMI, functionalized PEG and fluorescent lanthanide oxyfluoride nanocrystals, of a novel nanotheranostic shaped in flexible rods. This lanthanide-peptide nanorod or LProd of bionic nature exhibited significantly enhanced tumor-targeting and -imaging properties compared to its spherical counterpart. Importantly, LProd potently inhibited tumor growth in a mouse model of human colon cancer through activating tumor suppressor protein p53 via MDM2/MDMX antagonism, while maintaining a highly favorable biosafety profile. Our data demonstrate that LProd as a multifunctional theranostic platform is ideally suited for tumor-specific peptide drug delivery with real-time disease tracking, thereby broadly impacting clinical development of antitumor peptides.

---

[*] Corresponding author. phou@xjtu.edu.cn (P. Hou). [**] Corresponding author. wlu@ihv.umaryland.edu (W. Lu). [***] Corresponding author. mapx@umich.edu (P.X. Ma).

[1] These authors contributed equally to this work.

Appendix A. Supplementary data
Supplementary data related to this article can be found at https://doi.org/10.1016/j.biomaterials.2019.03.026.

Keywords

Peptide-based nanomedicines; Biomimetic nanomaterials; Self-assembled theranostic; Tumor targeting; Tumor imaging

1. Introduction

Nanomedicines have garnered significant attention recently due to their potential application in cancer therapy *via* the enhanced permeation and retention (EPR) effect [1]. Despite there have been a great number of successes of nanomedicine in cancer diagnosis and therapy, nanoparticles still face the inherent restriction of limited tumor accumulation. Suffered from the nonuniformly leaky vascular system and dense interstitial space at tumor sites, the uniform penetration of large nanotherapeutics (> 50 nm) is hydrodynamically and sterically slowed, sometimes even stopped [2,3]. Although this obstacle can be overcome by downscaling (< 30 nm), these smaller ones have to confront rapid clearance [4,5]. To reconcile this contradiction, tumor-microenvironment (TME) responsive nanoparticles were developed, whose physicochemical properties including size and charge can be precisely manipulated by the special conditions of TME [6,7]. Nevertheless, the uncertainty and complicacy of TME extremely likely result in the failure of TME response. Besides, additional instant-on response to TME steps will add indeterminacy for the efficacy of nanomedicines. Thus, it will be meaningful to develop more effective and reliable strategies to enhance the tumor-specific accumulation of nanomedicines.

Actually, in nature, a great number of pathogens such as viruses and bacteria have a soft claviform geometry at nano- or micro-scale, and they are always capable of high infiltration [8]. Inspired by this phenomenon, pioneering studies have reported that pathogens-like nanoparticles exhibit a strong ability of tumor enrichment and cellular internalization [9,10]. Despite some successful flexible rod-like nanoparticles assembled by polymers, all of them almost inevitably suffer from the unpredictable hydrophobic interference between drugs and carriers, resulting in the low drug loading (< 10%, w/w). This problem will be more acute for the macromolecular therapeutics, such as proteins and peptides [11,12]. In addition, commercial pathogens-like nanoparticles always fail to distinguish cancer cells from the noncancerous ones, thereby causing severe side effects and drug waste [7]. Thus, there is a compelling need to develop more effective bio-inspired rod-shaped theranostic platform with enhanced tumor specificity for cancer diagnosis and therapy.

To further push the boundary of nanomedicines, it is necessary to expand their application for modulating protein-protein interactions (PPIs), but not only focus them on traditional chemotherapy or gene therapy. It is the fact that human diseases including cancer are usually caused by aberrant PPIs [13], thus selectively interfering with functional PPIs will provide an effective strategy for disease control and therapy [14–16]. Owing to the finite area of interaction, traditional small-molecule drugs appear to be unsatisfactory for this purpose [17,18], while peptides are the perfect candidates to tackle this limitation as they are able to closely mimic the topological structure of proteins [19]. However, the main shortcoming of peptides is their low targeted internalization and short lifetime, which severely limits their clinical application. To capture their bioactivities, many strategies were developed to improve the stability and permeability of peptides, including, but not limited to, peptide cyclization, hydrocarbon stapling, liposomes or micelles encapsulation and nanoparticles conjugation [16,19–22]. However, all of the vehicle-free strategies are stymied by non-specific organ biodistribution, short circulation or un-monitored trafficking without tracking, and the vehicle-delivered strategies always suffer from the large and hydrophobic interfaces of peptides, resulting in the difficulty of being encapsulated or conjugated by vehicles [22,23]. Conceptually, *in vivo* viable targeted delivery systems with high loading and real-time tracking are thus urgently needed to accelerate the development of peptide drugs.

Towards this end, we developed a flexible lanthanide-peptide nanorod termed LProd, which was constructed by a thiol-induced molecular self-assembly, as a theranostic platform for cancer diagnosis and peptide-derived therapy (Fig. 1). Benefitted from large Stokes shift, high biocompatibility & stability, and strong fluorescent intensity, lanthanide-doped nanocrystals (LDNc) have been demonstrated to be widely used as imaging tools in life science and biomedicine [21,24]. For enhanced tumor targeting, a CD13-specific binding cyclopeptide iNGR (CRNGRGPDC) [25] was assembled at the surface of the LProd. In this study, a dodecameric peptide for p53 reactivation, termed PMI (TSFAEYWALLSP), was introduced into the LProd for anti-cancer therapy through antagonizing the interaction between p53-MDM2/MDMX [16,26,27]. Through fully nanostructure and biology studies, we demonstrated that LProd could be used as a potential agent for peptide-derived cancer diagnosis and therapy. More significantly, LProd can push the boundary of pathogens-like nanomedicines to peptide-derived cancer therapy and drug tracing, further reinvigorating the development of peptide drugs through targeting intracellular PPIs responsible for a great variety of human diseases including cancer.

2. Results and discussion

2.1. Preparation and characterization of LProd

The devised nanobacteria-like LProd can be synthesized quickly and conveniently by a two-step “one-pot” reaction between lanthanide-doped nanocrystals (named LDNc; GdOF: 45%Ce, 15%Tb), PMI, dimercapto polyglycol (SH-PEG-SH) and Sulfhydryl-PEGylated iNGR (iNGR-PEG-SH) (Fig. 1A). Luminescent LDNc capable of conjugating free sulfhydryl groups was synthesized as previously described [21,24], and reacted with hydrochloric acid (pH 4.0) to expose the surface [16,27]. iNGR was sulfhydryl-PEGylated to iNGR-PEG-SH for LDNcs conjugation. An extra Cys residue was also introduced to the *C*-terminus of PMI for peptide attachment. For LProd fabrication, luminescent LDNc capable of conjugating free sulfhydryl groups was firstly conjugated with cysteine-modified PMI to form LDNc-PMI as our previous studies [16,27], subsequently self-assembling with dimercapto polyglycol (SH-PEG-SH) and Sulfhydryl-PEGylated iNGR (iNGR-PEG-SH) into the flexible rod-shaped Lprod. In details, 5 mg of LDNc were dissolved in 10 mL of reaction buffer (20% acetonitrile and 80% standard PBS) containing 0.2 mM PMI-Cys to form LDNc-PMI. After a 20-min magnetic stirring, increased Zeta potential (Fig. 2A), characteristic IR (Fig. 2B) and UV absorbance (Fig. 2C) confirmed the formation of LDNc-PMI. Next, 1 mg of HS-PEG-SH (MW 2000) and 0.5 mg iNGR-PEG-SH (MW 3000) were added to cross-link LDNcs-PMI. After a 40-min incubation at 30 °C with stirring, ~7 mg of LProd were collected by centrifugation (the yield of ~65%). Similarly, a further increase in the Zeta potential demonstrated the conjugation of positively charged iNGR-PEG-SH (Fig. 2A). In addition, FTIR (Fig. 2B) and UV-Vis spectroscopy (Fig. 2C) also confirmed the conjugation of iNGR as evidenced by more sharp characteristic absorbance peaks given by peptide. To determine the efficiency of peptide loading in the nanorod, LProds were dissolved in PBS buffer containing 6 M guanidine hydrochloride and 50 mg/mL dithiothreitol to cleave the connection between sulfydryl (in mercapto PEG or PMI-Cys) and LDNc. As a result, 0.25 mmol/g (mmol/g = peptide molarity/LProd mass) of peptides were released (as quantified by HPLC, Fig. S1).

During the assembly between LDNc-PMI, HS-PEG-SH and iNGR-PEG-SH, LDNc-PMI were anchored each other through covalently connecting to the free thiol group in the HS-PEG-SH, while the mono-sulfhydryl PEG (iNGR-PEG-SH) could stop this crosslinking and expose the iNGR at the surface. In this process, the crosslinking elongation *via* HS-PEG-SH and termination by iNGR-PEG-SH occurred simultaneously, but at different frequencies, thereby causing the non-isotropic cross-bonding among LDNc-PMI particles and subsequently forming the ellipsoid-shaped LProd. In addition, owing to the flexible main chain of the PEG, LProd is expected to have a flexible construction, like the flexible skeleton of a bacterium. To address this, TEM image was taken and colored, in which as-prepared LProd nanoparticles had a bacteria-like morphology of irregular ellipsoid at nanoscale (Fig. 1B1). Measured by dynamic light scattering, mean hydrodynamic diameter of LProd is 160 nm with polydispersity index of ≈0.19 (Fig. S2), indicating the relatively narrow particle size distribution of LProd. To obtain the details about the flexible ellipsoid, LProd solution was probed by small angle X-ray scattering (SAXS), which is extremely sensitive to the flexible shape at nanoscale [28,29]. At a low concentration (0.1 mg/mL) of LProd, the electron-lucent non-metallic components (PEG and peptide) and bound water contribute ignorably to the SAXS diagram, thus the scattering spectra only reflected the undulations characteristic of the integral flexible LProd (Fig. 2D). Using an orientationally averaged rod model [29,30], the best fit yields that LProd was an irregularly elliptic shape with three half principal axes length of 11 nm, 51 nm and 91 nm (Fig. 2E and F), which were in agreement with those obtained from TEM images (Fig. 2G). When the concentration of LProd was increased to 1 mg/mL, the scattering spectra included the periodic undulations characteristic of nanoparticle inside the LProd (Fig. 2H). Fitted by an orientationally averaged sphere model, a positive peak at 4.1 nm and a negative hollow at 8.9 nm could be found in the SAXS studies (Fig. 2I). This indicated that the radius of nanocrystals (LDNc-PMI) was about 4.1 nm, and the interval between two nanocrystals was ~8.9nm (Fig. 2J), which was also consistent with the HRTEM image (Fig. 2K). Altogether, these data support that LProd has a nanobacteria-like flexible rods shape.

Next, we tested the colloidal stability of LProd and LDNc-PMI (0.1 mg/mL) in PBS buffer (5 mL, pH 7.4) at 37 °C. As expected, LProd kept monodisperse after a 24-h incubation, while LONc-PMI began to aggregate from 1 h (Fig. S3), indicating that peptide-derived PEGylation significantly improved particle stability and monodispersity. Besides, nanoparticle always adsorbed many biomolecules in especial of proteins, termed protein corona, resulting in the aggregation and charge reversal. This will cause nanoparticle losing its biofunction [31,32]. Thus, we expected that the sufficient PEGylation can increase the laziness of the LProd surface, thereby overcoming the effect of protein corona. To prove this, the colloidal stability of LProd (0.1 mg/mL) was tested again in PBS buffer (5mL, pH 7.4) containing 20% fetal calf serum (FBS) at 37 °C. As shown in Fig. S4A, LProd kept monodisperse after 12 h, while the agglutination occurred after a 24-h incubation. After a 12- and 24-h incubation, Zeta potentials of LProd were measured after centrifugation and resuspension in PBS buffer. The results showed that the potential at 12 h (25.9 mV) was close to the initial value of 26.1 mV (Fig. 2A), while the potential at 24 h occurred negatively shifted (Fig. S4B). Altogether, our data indicate that LProd has low protein adsorption, and can maintain stability in biological environment more than 12 h.

2.2. Glutathione-triggered “Off–On” release of peptide cargo from LProd

Given that glutathione (GSH), a tripeptide thiol, is widely present in the cytoplasm of live cells, particularly in cancer cells at millimolar range [33,34], thus LProd should be sensitive to intracellular GSH, thereby controlling the release of the peptide cargo. Indeed, after a 4-h reduction by PBS buffer (pH 7.4) containing 10 mM GSH, the LProd disassembled from nanorod shape to some monodispersed nanocrystal (Fig. 3A) with a significantly decreased hydrodynamic diameter (~10nm, Fig. 3B), demonstrating the stimuli-responsive disassembly process. After this process, the supernatant was subjected to HPLC analysis after 10000*g* centrifugation to remove solid nanoparticles. As shown in Fig. 3C, almost all PMI-SH were released from LProd after a 4-h reduction, while no peptides were released in the GSH-free control. To further explore the GSH-triggered release of peptide cargo, the release kinetics of PMI-Cys from LProd was monitored by HPLC during the process of disassembly triggered by 10 mM GSH. As shown in Fig. 3D, 50% PMI-Cys were released at 0.64 h, and > 90% peptides could be released at 2 h. In a sharp contrast, > 90% residual PMI-Cys were still present in LProd after a 12-h GSH-free incubation in PBS buffer (pH 7.4) (Fig. 3D). Taken together, our data demonstrate that peptide cargo loading in LProd exhibits an “Off–On” release behavior in the presence of GSH.

2.3. LProd specifically internalize into cancer cells via iNGR-Mediated cellular uptake

Cancer cell-specific cytomembrane penetrability is required for potent anti-tumor efficacy of pathogens-like LProd. To address this, a CendR tumor penetrating cyclopeptide iNGR (CRNGRGPDC) were introduced into the nanorod. The annular iNGR can specifically and rapidly bind to CD13, a zinc-dependent metalloproteinase, and trigger a proteolytic process to exposes the CendR motif (termed tNGR, seq.: CRNGR), thereby activating the CendR-mediated tumor penetrating process (Fig. 4A) [25]. To prove this, the FITC-labeled LProd was prepared using FITC-labeled PMI-Cys, and HCT116 cells were then incubated with 20 μg/mL PMI-Cys, LProd, LProd with tNGR (tNGR replaced iNGR during the LProd synthesis) or LProd without iNGR (HO-PEG-SH replaced iNGR-PEG-SH during the LProd synthesis) at pH 7.4 for 6 h. Expectedly, we observed a low-level cellular uptake of free PMI and LProd without iNGR, while LProd and its tNGR counterpart presented almost 100% of cellular internalization efficiency (Fig. 4B), indicating that iNGR can endow the LProd with cytomembrane penetrability *via* CendR-motif-mediated cellular internalization. To further validate this, 50 μM free iNGR peptides were pre-incubated to HCT116 cells for 12 h. As a result, cellular uptake of LProd was almost completely blocked (Fig. 4B). Considering that the iNGR/CendR-mediated cellular internalization is a process of actin-dependent micropinocytosis [25,35,36], 3 mM Amiloride (micropinocytosis inhibitor) and 2 μM cytochalasin D (actin inhibitor) were used to pre-incubate HCT116 cells, respectively. As expected, both of these two inhibitors sufficiently inhibited cellular uptake of LProd (Fig. 4B). Collectively, these data indicate that LProd can efficiently internalize into cancer cells *via* iNGR/CendR-mediated micropinocytosis.

Besides, iNGR and the flexible ellipse conformation can also endow the LProd with high specificity of cancer cells. First, CD13 has been demonstrated to be selectively overexpressed in tumor vascular cells and tumor cells [25,37,38]. Second, iNGR can be specifically proteolytically cleaved by a tumor-host protease to exposes the CendR motif, thereby avoiding the activation of internalization process in normal vasculature [25]. In addition, we found a very low level of cellular uptake when HCT116 cells were incubated with iNGR-free LProd for 6 h (Fig. 4B), presumably attributing to its special nanobacteria-like flexible rods shape. Next, suspension cultured peripheral blood mono-nuclear cells (PBMC) were used to simulate the process of non-cancerous cell internalization of LProd. After a 6-h incubation, the unassembled monomer, LDNc-PMI, which can relatively slowly penetrate into cancer cells (Fig. 4B), showed a high-level cellular uptake (82.6%, Fig. 4C), suggesting the potential side effects. In a sharp contrast, self-assembled LProd exhibited a low-level cellular internalization in PBMC, further supporting cancer cell specificity of LProd.

2.4. Cellular internalization of LProd is superior to its spherical counterpart

As mentioned above and the previous studies [25,37,38], iNGR has been demonstrated to enhance cancer cell-specific internalization of nanoparticles. Moreover, nanorods have a larger surface/volume ratio than nanospheres, improving the concentration of iNGR per unit volume of LProd. This will further enhance the uptake of cancer cells [9,39]. For comparison, we prepared a 74 nm-diameter spherical counterpart of LProd through assembling SH-PEG-SH and SH-PEG-iNGR in proper sequence, termed LPparticle (Fig. 5A–C). LPparticle had the same components and contents (LDNc-PMI, SH-PEG-SH and SH-PEG-iNGR) and similar volume ($\sim 2.14 \times 10^5$ nm^3) as LProd. Moreover, LPparticle was also capable of responding to GSH as LProd (Fig. S5). Meanwhile, our data showed that the superficial area of the LPparticle was 1.76×10^4 nm^2, which was about half of the LProd of 3.16×10^4 nm^2 (Fig. 5A–C). When HCT 116 cells were incubated with FITC-labeled spherical LPparticle or LPparticle without iNGR for 6 h, we observed higher cellular uptake of LPparticle (65.7%) than its iNGR-free counterpart (24.4%) (Fig. 5D and E). Under the same condition, LProd showed an almost complete cellular uptake by cancer cells relative to its iNGR-free counterpart (Fig. 5E). Altogether, our data indicate that nanoparticles with bacteria-like flexible rods shape and iNGR can significantly improve cancer cell-specific uptake.

Given that LDNc used in the present study can be simultaneously excited to green and red fluorescence [21,24]. Thus we expectedly observed cellular uptake of these two nanomedicines by receiving the LProd- or LPparticle-emissive fluorescence confocal laser scanning microscope (CLSM) (Fig. 5F). By semi-quantitating fluorescence intensity of

LProd- and LPparticle-treated HCT116 cells in Fig. 5F, we found that the unit fluorescence intensity of LProd was 1.5-fold higher than that of LPparticle (Fig. 5G), further supporting that nanobacteria-like flexible rods shape can enhance cancer cell-specific uptake of LProd.

2.5. LProd has more superior cancer-specific accumulation and tumor imaging than its spherical counterpart

In vivo biodistributions of LPparticle, LProd and LProd without iNGR in normal organs and tumor sites were assessed using HCT116 cell-derived xenograft tumor model (Fig. 6A). Four hours after intraperitoneal injection, organs and tumors were isolated and subjected to a quantified region-of-interest (ROI) analysis, as shown the organ average fluorescence intensity in Fig. 6B. Compared to its iNGR-deficient counterpart, LProd exhibited higher accumulation in the tumor sites, while showed a relatively low-level accumulation in heart, liver, spleen, lung and kidney (Fig. 6B), indicating that iNGR significantly improves tumor targeting of LProd. To compare tumor specificity between LPparticle and LProd, the ratios of tumor/organ for LPparticle (gray bars) and LProd (red bars) were calculated in Fig. 6C. As expected, LProd showed higher tumor accumulation over healthy organs, suggesting that flexible rod-shaped nanotherapeutics may have high tumor targetability in comparison with conventional spherical nanomedicines.

Considering that LProd has excellent tumor-specific accumulation and the potential of fluorescence imaging, thus we speculate that LProd can be used for cancer diagnosis. To prove this, tumor accumulation of LProd and LPparticle was longitudinally monitored for up to 12 h using fluorescence reflectance imaging. As shown in Fig. 6D, the fluorescence of LPparticle could be clearly observed at 4 h after intraperitoneal injection, while the accumulation of LProd was relatively slow. However, after 12 h postinjection, fluorescent signal of LPparticle became weaker, while that of LProd became stronger at the tumor sites relative to 4 h after injection (Fig. 6D). Further statistical analysis revealed that the fluorescence intensity of LProd at 12 h was ~2.5-fold higher than LPparticle, as shown in Fig. 6E. Taken together, our data indicate that LProd as a long-acting tumor imaging tool can be used for cancer diagnosis and drug tracking *in vivo*.

2.6. Potent in vivo anti-tumor efficacy of LProd

HCT116 p53$^{+/+}$ cell-drived xenograft tumor model was established to test *in vivo* anti-cancer efficacy of LProd. Briefly, 10 days after inoculation, mice were randomly divided into five groups (n = 5/group), and then subjected to 6 different treatments by the intraperitoneal injection of PBS, 1.5 mg/kg doxorubicin, 1.5 mg/kg PMI, 1.5 mg/kg LProd, 1.5 mg/kg Lrod (the PMI-deficient counterpart of LProd) and 1.5 mg/kg LPparticle (Fig. 7A). The results showed that, 5 days after the first treatment, there was a significant difference in tumor volume between LProd-treated mice and control mice, and the difference became more significant over time (Fig. 7B). In addition, we also found that, starting from the 7 t h day, there existed a gradually expand difference in tumor volume between LProd- and LPparticle-treated mice (Fig. 7B). At the 13 t h day, all mice were euthanized, and tumors were then isolated and weighed. As shown in Fig. 7C, the weight of xenograft tumors from LProd-treated mice was 12.3 times lower than that of control mice, 4.1 times lower than that of DOX-treated mice, ~11.0 times lower than that of PMI- or Lrod-treated mice, and 2.0 times lower than that of LPparticle-treated mice. Notably, there was no significant difference between free PMI treated-mice and control mice, indicating that free PMI can not be delivered into cancer cells. H&E and TUNEL staining further supported the above conclusions (Fig. 7D and E). Altogether, our data demonstrate potent *in vivo* anti-tumor efficacy of LProd, which is superior to its spherical counterpart.

2.7. LProd exerts its anti-tumor role through p53 reactivation

Our previous studies have demonstrated that intracellular PMI in nanomolar range can reactivate p53 to induce cancer cell apoptosis [16,27,40]. Thus, to comparatively assess anti-tumor activity of nanobacteria-like nanorod *in vitro*, 250 nM LProd, LPparticle, free PMI or 5 μM Nutlin 3 (a small-molecule agonist of MDM2 as a positive control) were used to treat HCT116 p53$^{+/+}$ or HCT116 p53$^{-/-}$ cells for 3 days. As expected, both of LProd and LPparticle could awake the function of PMI-SH to induce cell apotosis in a p53-dependent manner, like Nutlin3 (Fig. 8A and B). By statistically analyizing multiple parallel trials, we found that the potency of LProd was significantly superior to that of LPparticle (Fig. 8C), which is presumably because that the nanobacteria-like flexible rods shape can increase cancer cell-specific uptake of LProd.

Besides, PMI has been demonstrated to be capable of reactivating p53 through blocking its interaction with MDM2/MDMX, and subsequently elevating p21 expression (Fig. 9A) [16,27]. Thus, to determine anti-tumor mechanism of LProd, we performed a series of IHC assays in xenograft tumors using p53 and p21 antibodies. The results showed that the levels of p53 and p21 were significantly elevated in the LProd- or LPparticle-treated tumors in compasion with PBS- or PMI-treated ones, particularly in LProd-treated tumors (Fig. 9B and C). In addition, we also determined proliferative ability of xenograft tumors by Ki67 (a marker of proliferation) staining. As expected, relative to PBS-/PMI-treated tumors, even LPparticle-treated tumors, LProd-treated tumors showed a signifcant reduction in the percentage of Ki67-positive cells (Fig. 9D). Collectively, our data indicate that LProd can inhibit tumor growth through p53 reactivation.

2.8. In vivo safety evaluation of LProd

It is the fact that the freely distributed drugs and carrier outside tumor sites can result in upsetted circadian rhythm and castrated curative effect as a consequence of poor tumor specificity [41]. To minimize side effects, a two-stage targeting strategy was adopted in LProd (Fig. 10A). Aided by the endothelial leakiness of nanoparticles, termed NanoEL (first targeting) [42–45], LProd can similarly concentrate at the tumor sites. Moreover, iNGR conjugation and increased iNGR concentration per unit volume attributed to the nanobacteria-like structure further improved the tumor targeting of LProd. This will greatly decrease the number of off-target drugs, thereby eliminating the side effects. In addition, there is evidence proving that LDNc is essentially biocompatible and non-cytotoxic for biomedical applications [16,21,24], further ensuring the safety of LProd.

Next, to explore its biosafety, we carried out comprehensive toxicity testing during and after the adminstration. During a 13-day administration, we did not find weight loss in PMI-, LProd- and LPparticle-treated mice, while body weight was obviously decreased in DOX-treated mice (Fig. S6). More seriously, DOX-treated mice were diagnosed with leukopenia and thrombopenia (Fig. S7), a medium liver spotty necrosis (Fig. 10B–E), the symptoms of glomerular lesions (Fig. 9F) and spleen failure (Fig. 10G and H). On the contrary, LProd treatment almost did not affect the health of mice (Fig. 10B–H). Notably, LPpariticle-treated mice presented a low-level hepatic and renal failure, which was completely avoided in LProd-treated mice (Fig. 10B–H). Besides, all mice were not diagnosed with any other common side effects as a result of drug toxicities, such as myocardial damage (Fig. 10I and J), allergic lung resistance (Fig. 10K) and acute sepsis (Fig. S8). Overall, our data demonstrate that LProd is sufficiently safe, and indicate that nanomedicines with nanobacteria-like structure have a higher biosafety than spherical ones,.

3. Conclusion

In summary, our data demonstrate that the presented nanosystem with flexible rods shape can more effectively deliver PMI into tumor sites, and more potently inhibit tumor growth *in vitro* and *in vivo* through reactivating p53 signaling compared to its spherical counterpart. This work will provide a compelling case for the use of PMI-based therapies in cancer patients carrying wild-type p53, while tracing the therapeutic agents *via* fluorescence imaging. Importantly, nanobacteria-like flexible rods designed in the present study is convenient for preparation *via* a one-pot self-assembly of LDNc, peptide cargo and functional PEG. The nanorod exhibits enhanced capacity for tumor targeting, imaging and killing, while largely eliminates the systemic toxicity. Thus, LProd can serve as a desirable multifunctional theranostic platform for hazard-free cancer therapy and drug tracing. Moreover, considering these superior properties from the special topological structure of LProd, bionic flexible rod-shaped nanotherapeutics may be more effective for cancer therapy than the currently approved spherical nanomedicines.

4. Experimental section

4.1. Synthesis of peptides (PMI-Cys and iNGR)

All peptides were synthesized on rink amino MBHA resins by Fmoc chemistry as our previous reports [46–48]. After synthesis, peptides were cleaved by a reagent cocktail, which is consist of TFA (88%), phenol (5%), H2O (5%) and TIPS (2%). Next, products were identified and purified by C18 or C4 reversed-phase HPLC [49]. ESI-MS was used to ascertain the molecular weights of peptides.

4.2. Fabrication of LProd and LPparticle

First, 5 mg of LDNc were dissolved in 10 mL of reaction buffer (20% acetonitrile and 80% standard PBS) containing 0.2 mM PMI-Cys to form LDNc-PMI after a 20-min magnetic stirring. Second, 1 mg of HS-PEG-SH (MW 2000) and 0.5 mg iNGR-PEG-SH (MW 3000) were added to crosslink LDNcs-PMI. After a 40-min incubation at 30 °C with stirring, ~7 mg of LProd could be collected by centrifugation (the yield of ~65%>). As for the LProd without iNGR, iNGR-PEG-SH was replaced by NH2-PEG-SH (MW 2000Da), and everything else was the same as the protocol of LProd.

For the fabrication of LPparticle, 1 mg HS-PEG-SH solution was added into 10 mL LDNc-PMI solution (0.5mg/mL in PBS, pH7.4) for further functionalized reaction at 30 °C for 1 h. After then, 0.5 mg of sulfhydryl-PEGylated targeting peptide iNGR-PEG-SH was added to the mixture to saturate the free sulfhydryl groups at the surface of the spheroidal nanostructure. After a 40-min incubation at 35 °C with stirring, ~7.5 mg of LPparticle were collected by 10000*g* centrifugation (the yield of ~70%).

4.3. Physicochemical properties of LProd, LPparticle and LDNc

The morphology and lattice structure were observed on high-resolution transmission electron microscope (HRTEM, F20, FEI) at 200 kV, or transmission electron microscope at 100 kV as our previous reports [16,50]. The hydrodynamic size distribution, zeta potential measurement, Fourier transform infrared (FT-IR) spectroscopy and UV-vis absorption spectra were measured as our previously reported protocols.

Supplementary Material

Refer to Web version on PubMed Central for supplementary material.

Acknowledgments

This work was supported by the Clinical Research Award of the First Affiliated Hospital of Xi'a Jiaotong University (No. XJTU1AF-CRF-2017–003 to P Hou and W He), the National Natural Science Foundation of China (No. 81572627 to P Hou), and NIH R01CA219150 (to W Lu), and the Fundamental Research Funds for the Central Universities (No. Z201404078 to L Wang).

References

[1]. Wilhelm S, Tavares AJ, Dai Q, Ohta S, Audet J, Dvorak HF, Chan WC, Analysis of nanoparticle delivery to tumours, Nat. Rev. Mater 1 (5) (2016) 16014.

[2]. Tang L, Yang X, Yin Q, Cai K, Wang H, Chaudhury I, Yao C, Zhou Q, Kwon M, Hartman JA, Investigating the optimal size of anticancer nanomedicine, Proc. Natl. Acad. Sci. U. S. A 111 (43) (2014) 15344–15349. [PubMed: 25316794]

[3]. Dreher MR, Liu W, Michelich CR, Dewhirst MW, Yuan F, Chilkoti A, Tumor vascular permeability, accumulation, and penetration of macromolecular drug carriers, J. Natl. Cancer Inst 98 (5) (2006) 335–344. [PubMed: 16507830]

[4]. Chauhan VP, Stylianopoulos T, Martin JD, Popović Z, Chen O, Kamoun WS, Bawendi MG, Fukumura D, Jain RK, Normalization of tumour blood vessels improves the delivery of nanomedicines in a size-dependent manner, Nat. Nanotechnol 7 (6) (2012) 383–388. [PubMed: 22484912]

[5]. Choi HS, Liu W, Liu F, Nasr K, Misra P, Bawendi MG, Frangioni JV, Design considerations for tumour-targeted nanoparticles, Nat. Nanotechnol 5 (1) (2010) 42. [PubMed: 19893516]

[6]. Ge Z, Liu S, Functional block copolymer assemblies responsive to tumor and intracellular microenvironments for site-specific drug delivery and enhanced imaging performance, Chem. Soc. Rev 42 (17) (2013) 7289–7325. [PubMed: 23549663]

[7]. Han K, Zhang J, Zhang W, Wang S, Xu L, Zhang C, Zhang X, Han H, Tumor-triggered geometrical shape switch of chimeric peptide for enhanced in vivo tumor internalization and photodynamic therapy, ACS Nano 11 (3) (2017) 3178–3188. [PubMed: 28296387]

[8]. Geisbert TW, Jahrling PB, Exotic emerging viral diseases: progress and challenges, Nat. Med 10 (12s) (2004) S110. [PubMed: 15577929]

[9]. Chauhan VP, Popović Z, Chen O, Cui J, Fukumura D, Bawendi MG, Jain RK, Fluorescent nanorods and nanospheres for real-time in vivo probing of nanoparticle shape-dependent tumor penetration, Angew. Chem. Int. Ed 50 (48) (2011) 11417–11420.

[10]. Li D, Tang Z, Gao Y, Sun H, Zhou S, A bio-inspired rod-shaped nanoplatform for strongly infecting tumor cells and enhancing the delivery efficiency of anticancer drugs, Adv. Funct. Mater 26 (1) (2016) 66–79.

[11]. Lee SJ, Koo H, Jeong H, Huh MS, Choi Y, Jeong SY, Byun Y, Choi K, Kim K, Kwon IC, Comparative study of photosensitizer loaded and conjugated glycol chitosan nanoparticles for cancer therapy, J. Control. Release 152 (1) (2011) 21–29. [PubMed: 21457740]

[12]. Liu K, Xing R, Zou Q, Ma G, Möhwald H, Yan X, Simple peptide-tuned self--assembly of photosensitizers towards anticancer photodynamic therapy, Angew. Chem 128 (9) (2016) 3088–3091.

[13]. Zhao Y, Aguilar A, Bernard D, Wang S, Small-molecule inhibitors of the MDM2-p53 protein-protein interaction (MDM2 Inhibitors) in clinical trials for cancer treatment: miniperspective, J. Med. Chem 58 (3) (2014) 1038–1052. [PubMed: 25396320]

[14]. Keskin O, Gursoy A, Ma B, Nussinov R, Principles of protein – protein interactions: what are the preferred ways for proteins to interact, Chem. Rev 108 (4) (2008) 1225–1244. [PubMed: 18355092]

[15]. Spring DR, Chemical genetics to chemical genomics: small molecules offer big insights, Chem. Soc. Rev 34 (6) (2005) 472–482. [PubMed: 16137160]

[16]. Yan J, He W, Yan S, Niu F, Liu T, Ma B, Shao Y, Yan Y, Yang G, Lu W, Self-assembled peptide-lanthanide nanoclusters for safe tumor therapy: overcoming and utilizing biological barriers to peptide drug delivery, ACS Nano 12 (2) (2018) 2017–2026. [PubMed: 29376322]

[17]. Zinzalla G, Thurston DE, Targeting protein-protein interactions for therapeutic intervention: a challenge for the future, Future Med. Chem 1 (1) (2009) 65–93. [PubMed: 21426071]

[18]. Vanhee P, van der Sloot AM, Verschueren E, Serrano L, Rousseau F, Schymkowitz J, Computational design of peptide ligands, Trends Biotechnol 29 (5) (2011) 231–239. [PubMed: 21316780]

[19]. Nevola L, Giralt E, Modulating protein-protein interactions: the potential of peptides, Chem. Commun 51 (16) (2015) 3302–3315.

[20]. Sewald N, Jakubke H-D, Peptides: Chemistry and Biology, John Wiley & Sons, 2015.

[21]. Yan J, He W, Li N, Yu M, Du Y, Lei B, Ma PX, Simultaneously targeted imaging cytoplasm and nucleus in living cell by biomolecules capped ultra-small GdOF nanocrystals, Biomaterials 59 (2015) 21–29. [PubMed: 25941998]

[22]. Acar H, Ting JM, Srivastava S, LaBelle JL, Tirrell MV, Molecular engineering solutions for therapeutic peptide delivery, Chem. Soc. Rev 46 (21) (2017) 6553–6569. [PubMed: 28902203]

[23]. Fosgerau K, Hoffmann T, Peptide therapeutics: current status and future directions, Drug Discov. Today 20 (1) (2015) 122–128. [PubMed: 25450771]

[24]. Zhang J, Yan J, Yang Q, Yan Y, Li S, Wang L, Li C, Lei B, Yang G, He W, Arginine-modified dual emission photoluminescent nanocrystals for bioimaging at subcellular resolution, J. Biomater. Appl 32 (4) (2017) 533–542. [PubMed: 28799820]

[25]. Alberici L, Roth L, Sugahara KN, Agemy L, Kotamraju VR, Teesalu T, Bordignon C, Traversari C, Rizzardi G-P, Ruoslahti E, De novo design of a tumor-penetrating peptide, Cancer Res 73 (2) (2013) 804–812. [PubMed: 23151901]

[26]. Pazgier M, Liu M, Zou G, Yuan W, Li C, Li C, Li J, Monbo J, Zella D, Tarasov SG, Structural basis for high-affinity peptide inhibition of p53 interactions with MDM2 and MDMX, Proc. Natl. Acad. Sci. U. S. A 106 (12) (2009) 4665–4670. [PubMed: 19255450]

[27]. Niu F, Yan J, Ma B, Li S, Shao Y, He P, Zhang W, He W, Ma PX, Lu W, Lanthanide-doped nanoparticles conjugated with an anti-CD33 antibody and a p53-activating peptide for acute myeloid leukemia therapy, Biomaterials 167 (2018) 132–142. [PubMed: 29571049]

[28]. Gómez-Graña S, Hubert F, Testard F, Guerrero-Martínez A.s., Grillo I, Liz-Marzán LM, Spalla O, Surfactant (bi) layers on gold nanorods, Langmuir 28 (2) (2011) 1453–1459. [PubMed: 22165910]

[29]. Li T, Senesi AJ, Lee B, Small angle X-ray scattering for nanoparticle research, Chem. Rev 116 (18) (2016) 11128–11180. [PubMed: 27054962]

[30]. Ingham B, X-ray scattering characterisation of nanoparticles, Crystallogr. Rev 21 (4) (2015) 229–303.

[31]. Lundqvist M, Stigler J, Cedervall T, Berggård T, Flanagan MB, Lynch I, Elia G, Dawson K, The evolution of the protein corona around nanoparticles: a test study, ACS Nano 5 (9) (2011) 7503–7509. [PubMed: 21861491]

[32]. Monopoli MP, Walczyk D, Campbell A, Elia G, Lynch I, Baldelli Bombelli F, Dawson KA, Physical – Chemical aspects of protein corona: relevance to in vitro and in vivo biological impacts of nanoparticles, J. Am. Chem. Soc 133 (8) (2011) 2525–2534. [PubMed: 21288025]

[33]. Ock K, Jeon WI, Ganbold EO, Kim M, Park J, Seo JH, Cho K, Joo S-W, Lee SY, Real-time monitoring of glutathione-triggered thiopurine anticancer drug release in live cells investigated by surface-enhanced Raman scattering, Anal. Chem 84 (5) (2012) 2172–2178. [PubMed: 22280519]

[34]. Wang X, Cai X, Hu J, Shao N, Wang F, Zhang Q, Xiao J, Cheng Y, Glutathione-triggered “off–on” release of anticancer drugs from dendrimer-encapsulated gold nanoparticles, J. Am. Chem. Soc 135 (26) (2013) 9805–9810. [PubMed: 23789713]

[35]. Bian Z, Yan J, Wang S, Li Y, Guo Y, Ma B, Guo H, Lei Z, Yin C, Zhou Y, Liu M, Tao K, Hou P, He W, Awakening p53 in vivo by D-peptides-functionalized ultra-small nanoparticles: overcoming biological barriers to D-peptide drug delivery, Theranostics 8 (19) (2018) 5320–5335. [PubMed: 30555549]

[36]. Tashima T, Effective cancer therapy based on selective drug delivery into cells across their membrane using receptor-mediated endocytosis, Bioorg. Med. Chem. Lett 28 (18) (2018) 3015–3024. [PubMed: 30031619]

[37]. Kang T, Gao X, Hu Q, Jiang D, Feng X, Zhang X, Song Q, Yao L, Huang M, Jiang X, iNGR-modified PEG-PLGA nanoparticles that recognize tumor vasculature and penetrate gliomas, Biomaterials 35 (14) (2014) 4319–4332. [PubMed: 24565520]

[38]. An S, Jiang X, Shi J, He X, Li J, Guo Y, Zhang Y, Ma H, Lu Y, Jiang C, Single-component self-assembled RNAi nanoparticles functionalized with tumor-targeting iNGR delivering abundant siRNA for efficient glioma therapy, Biomaterials 53 (2015) 330–340. [PubMed: 25890731]

[39]. Park JH, von Maltzahn G, Zhang L, Derfus AM, Simberg D, Harris TJ, Ruoslahti E, Bhatia SN, Sailor MJ, Systematic surface engineering of magnetic nanoworms for in vivo tumor targeting, Small 5 (6) (2009) 694–700. [PubMed: 19263431]

[40]. He W, Yan J, Sui F, Wang S, Su X, Qu Y, Yang Q, Guo H, Ji M, Lu W, Shao Y, Hou P, Turning a Luffa protein into a self-assembled biodegradable nanoplatform for multitargeted cancer therapy, ACS Nano 12 (11) (2018) 11664–11677. [PubMed: 30335959]

[41]. Khanna I, Drug discovery in pharmaceutical industry: productivity challenges and trends, Drug Discov, Today Off 17 (19–20) (2012) 1088–1102.

[42]. Peng F, Setyawati MI, Tee JK, Ding X, Wang J, Nga ME, Ho HK, Leong DT, Nanoparticles promote in vivo breast cancer cell intravasation and extravasation by inducing endothelial leakiness, Nat. Nanotechnol 14 (3) (2019) 279–286. [PubMed: 30692675]

[43]. Tee JK, Setyawati MI, Peng F, Leong DT, Ho HK, Angiopoietin-1 accelerates restoration of endothelial cell barrier integrity from nanoparticle-induced leakiness, Nanotoxicology (2019) 1–19.

[44]. Wang J, Zhang L, Peng F, Shi X, Leong DT, Targeting endothelial cell junctions with negatively charged gold nanoparticles, Chem. Mater 30 (11) (2018) 3759–3767.

[45]. Setyawati MI, Tay CY, Chia SL, Goh SL, Fang W, Neo MJ, Chong HC, Tan SM, Loo SCJ, Ng KW, Xie JP, Ong CN, Tan NS, Leong DT, Titanium dioxide nanomaterials cause endothelial cell leakiness by disrupting the homophilic interaction of VE-cadherin, Nat. Commun 4 (2013) 1673. [PubMed: 23575677]

[46]. He W, Mazzuca P, Yuan W, Varney K, Bugatti A, Cagnotto A, Giagulli C, Rusnati M, Marsico S, Diomede L, Identification of amino acid residues critical for the B cell growth-promoting activity of HIV-1 matrix protein p17 variants, BBA-Gen. Subjects 1863 (1) (2019) 13–24.

[47]. Yu M, Yan J, He W, Li C, Ma PX, Lei B, Synthetic θ-defensin antibacterial peptide as a highly efficient nonviral vector for redox-responsive miRNA delivery, Adv. Biosyst 1 (12) (2017) 1700001.

[48]. He W, Yan J, Jiang W, Li S, Qu Y, Niu F, Yan Y, Sui F, Wang S, Zhou Y, Peptide-induced self-assembly of therapeutics into a well-defined nanoshell with tumor-triggered shape and charge switch, Chem. Mater 30 (20) (2018) 7034–7046.

[49]. He W, Wang S, Yan J, Qu Y, Jin L, Sui F, Li Y, You W, Yang G, Yang Q, Ji M, Shao Y, Ma PX, Lu W, Hou P, Self-assembly of therapeutic peptide into stimuli-responsive clustered nanohybrids for cancer-targeted therapy, Adv. Funct. Mater 29 (10) (2019) 1807736.

[50]. He W, Huang H, Yan J, Zhu J, Photocatalytic and antibacterial properties of Au-TiO2 nanocomposite on monolayer graphene: from experiment to theory, J. Appl. Phys 114 (20) (2013) 204701.

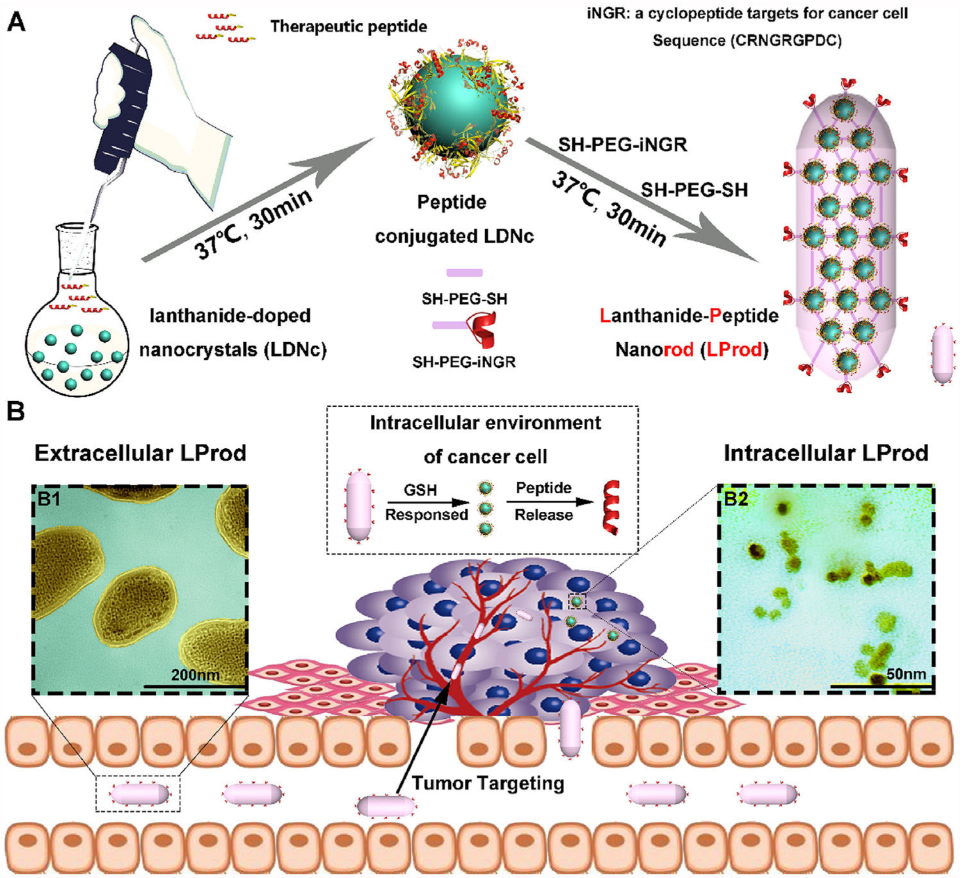

Fig. 1. Design and synthesis of nanobacteria-like LProd.

(**A**) Schematic depiction for the synthesis of nanobacteria-like LProd. (**B**) Schematic illustration for the function of nanobacteria-like LProd: 1) LProd can enrich in the tumor sites specifically by the EPR effect and iNGR active targeting; 2) LProd is sensitive to intracellular redox milieu to control the release of peptide cargo. The colored transmission electron micrograph (TEM) images of extracellular LProd (**B1**) and its reduced form after response to intracellular redox milieu (**B2**). The LProd was colored in yellow and the background in baby blue. (For interpretation of the references to color in this figure legend, the reader is referred to the Web version of this article.)

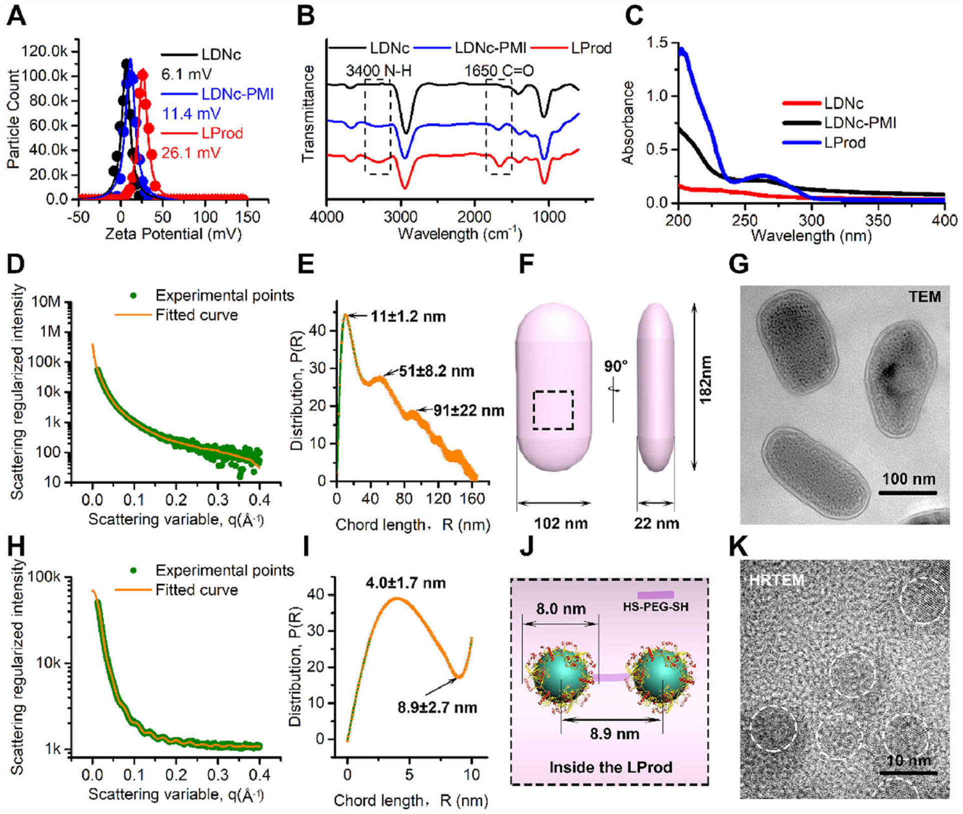

Fig. 2. Characterization of LProd.

(**A**) The surface charge (Zeta potential) of LDNc, LDNc-PMI and LProd measured in PBS buffer (pH 7.4) by DLS at 37 °C. All data points were the average of 20 measurements and were fitted by to a Gaussian distribution. (**B**) FT-IR spectroscopy of LDNc, LDNc-PMI and LProd. (**C**) UV-vis absorption spectra of LDNc, LDNc-PMI and LProd. (**D**) Small angle X-ray scattering (SAXS) diffractograms of LProd measured at the concentration of 0.1 mg/mL in PBS. The orange line is the least squares fit to the data (green points) using a rod model. (**E**) Corresponding chord length distributions calculated from (**D**). P (r) = chord length distribution function; R = radius. (**F**) The schematic illustration of nanobacteria-like LProd size, which was obtained from (**E**). (**G**) TEM image of LProd taken at 100 kV. (**H**) SAXS diffractograms of 1 mg/mL LProd in PBS. The orange line is the least squares fit to the data (green points) using a sphere model. (**I**) Corresponding chord length distributions calculated from (H). (**J**) Internal morphology of LProd obtained from (**I**). (**K**) High-resolution TEM (HRTEM) image of LProd taken at 300 kV. (For interpretation of the references to color in this figure legend, the reader is referred to the Web version of this article.)

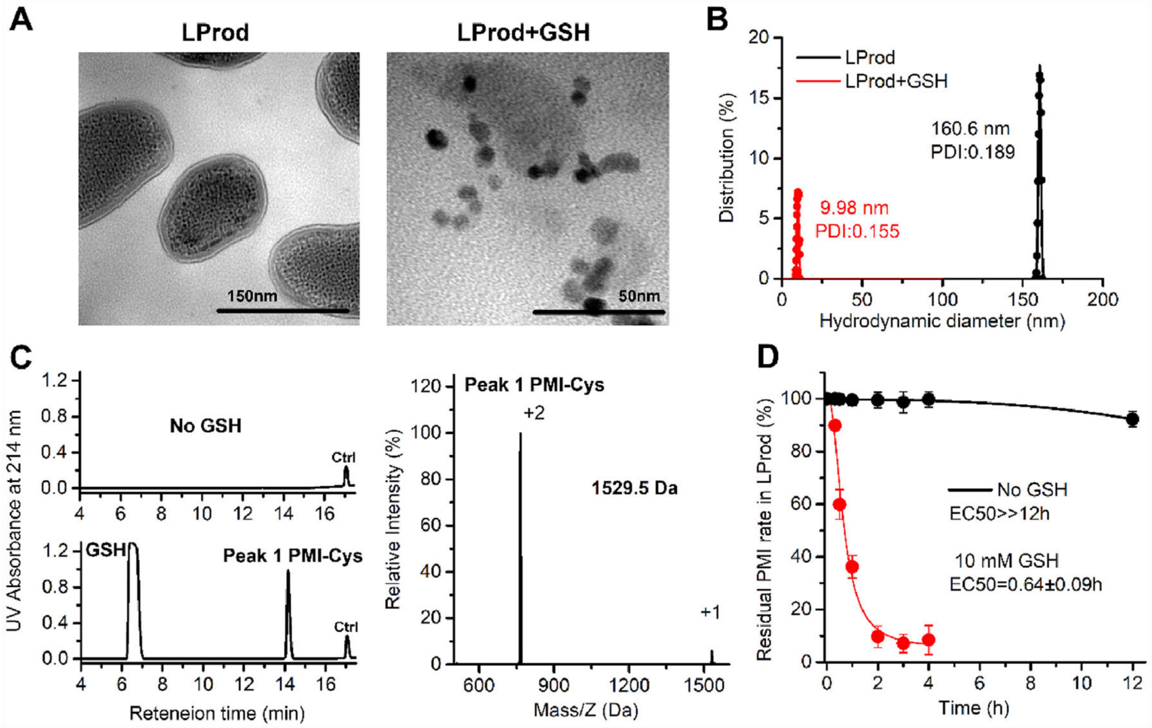

Fig. 3. Glutathione-triggered release of peptide cargo from LProd.

(**A**) TEM image of LProd before and after a 4-h reduction by 10 mM GSH. (**B**) Distributions of hydrodynamic diameter of LProd (the presence of GSH or not) measured by DLS. (**C**) LProd was incubated in PBS solution (pH 7.4), and no released peptide was detected in the supernatant (10000g centrifugation) after a 4-h incubation. LProd was incubated in intracellular-redox milieu-mimic PBS solution (10 mM GSH, pH7.4), and released peptide peak was detected in the supernatant (10000*g* centrifugation) after a 4-h incubation. A 22-mer peptide (Seq.: EIYIAQELRRIGDEFN-AYYA) was used as internal reference, termed Ctrl, and its retention time was about 17 min. The peak 1 is the PMI checked by ESI-MASS. (**D**) PMI-Cys release from LProd in intracellular redox environment mimic solution (including 10 mM GSH) or GSH-free solution quantified by HPLC.

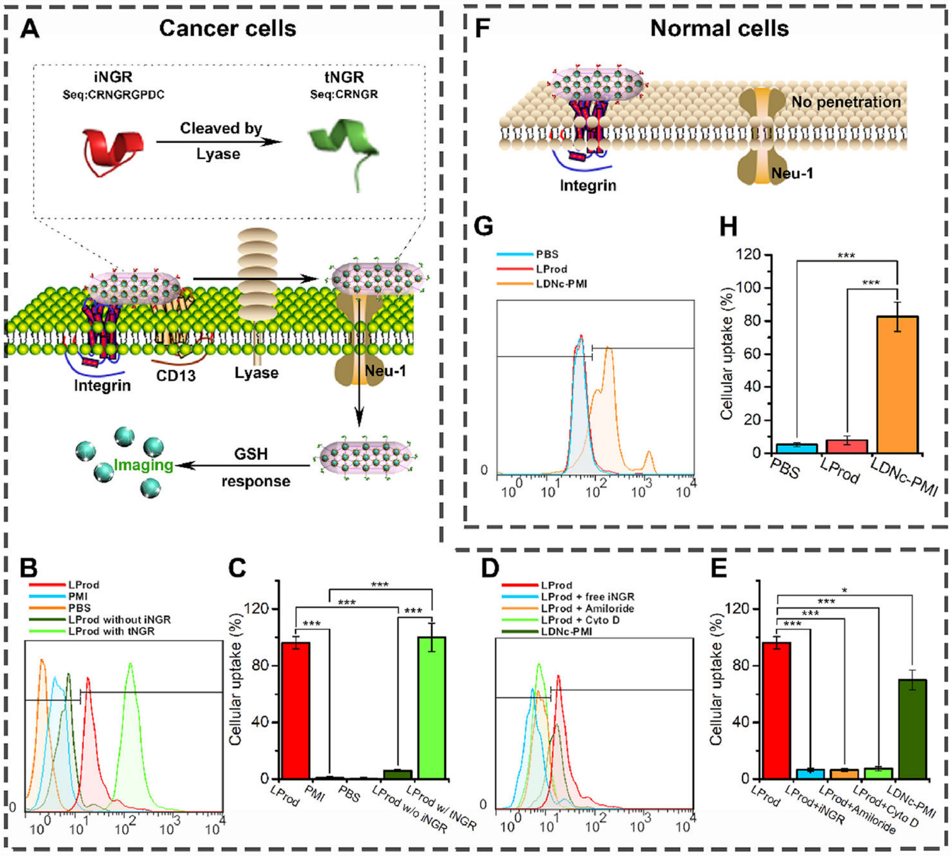

Fig. 4. LProd specifically internalizes into cancer cell *via* iNGR-mediated cellular micropinocytosis.

(**A**) Schematic depiction of the mechanism how iNGR conjugation enhances tumor targeting of LProd. (**B**) Cellular uptake of FITC-labled LProd, PMI, LProd without iNGR and LProd with tNGR into HCT116 cells measured by flow Cytometer. (**C**) Statistical analysis of the results in (**B**) (n = 3). (**D**) Cellular uptake of FITC-labeled LProd, with or without free iNGR, Amiloride or Cyto D preincubation into HCT116 cells. (**E**) Statistical analysis of the results in (**D**) (n = 3). (**F**) Schematic diagram and measurement of the LProd internalization into noncancerous cells. (**G**) Cellular uptake of FITC-labled LProd and LDNc-PMI into HCT116 cells measured by flow Cytometer. (**H**) Statistical analysis of the results in (**G**) (n = 3). *P* values were calculated by *t*-test (*, $p < 0.05$; **, $p < 0.01$; ***, $p < 0.001$).

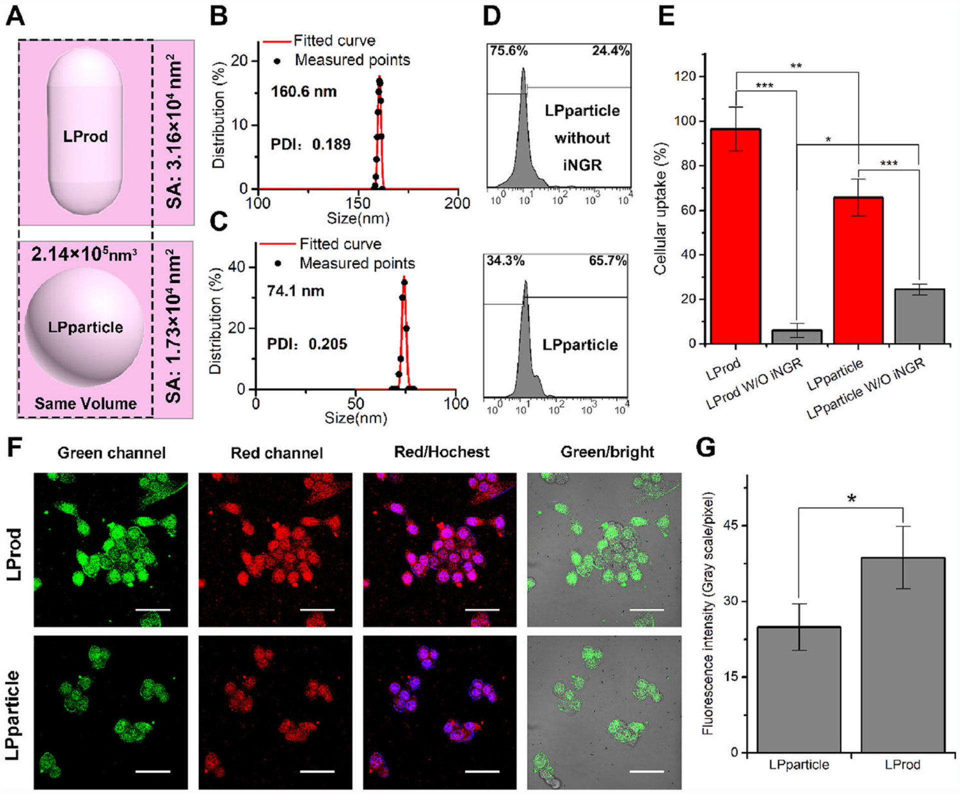

Fig. 5. Cellular internalization of LProd and its spherical counterparts.

(**A**) Schematic depiction of the morphology of LProd and LPparticle. Distributions of hydrodynamic diameter of LProd (**B**) and LPparticle (**C**) measured by DLS. (**D**) Cellular uptake of LPparticle *in vitro* measured by flow Cytometer. (**E**) Statistical analysis of cellular uptake rate of LProd, LProd without iNGR, LPparticle, and LPparticle without iNGR. (**F**) Cellular uptake analysis of LProd in HCT116 cells by confocal laser scanning microscope (CLSM). CLSM images of HCT116 cells after a 6-h incubation with 200 nM LProd or LPparticle. All images were taken under the same exciting light and detector gain (scale bar: 60 μm). (**G**) Semi-quantitating the unit fluorescence intensity of LProd- and LPparticle-treated HCT116 cells in (**F**).

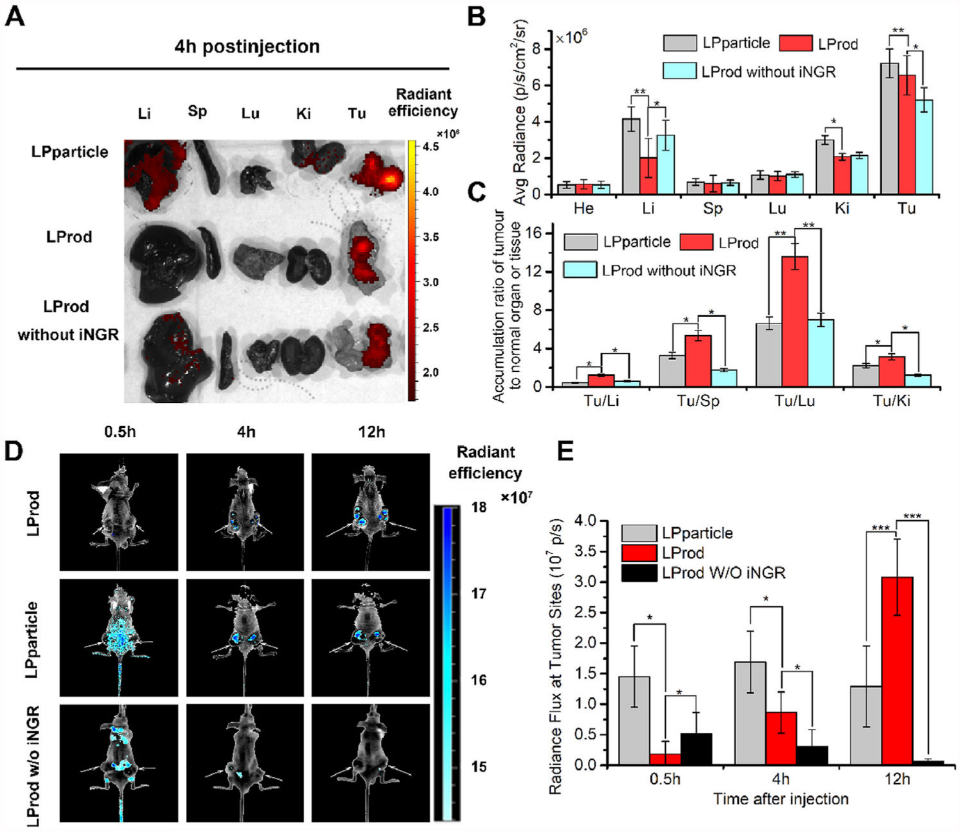

Fig. 6. Enhanced *in vivo* tumor imaging of LProd.

(**A**) Representative *ex vivo* fluorescent image of major organs and tumor sites at 4 h after intravenous injection of Lprod, LPparticle, or LProd without iNGR in HCT116 tumor-bearing mice (dose: 100 μg of per mouse). Li, liver; Sp, spleen; Lu, lung; Ki, kidneys; Tu, tumor. (**B**) Region-of-interest (ROI) analysis of the *ex vivo* fluorescent data as shown in (**A**). (n = 3/group, mean ± s.d.). Average accumulation of Lprod, LPparticle, and LProd without iNGR in heart (He), liver (Li), splees (Sp), lung (Lu), kidney (Ki) and tumor (Tu) at 4 h post-injection. (**C**) Tumor-to-background (normal organ or tissue) ratios for LPparticle, LProd and LProd without iNGR at 4 h post-injection. LProd showed improved tumor selectivity over the surrounding normal organs or tissues, compared to LPparticle or LProd without iNGR. (**D**) Fluorescence images of LProd, LPparticle and LProd w/o iNGR *in vivo*. Fluorescence images of LProd, LPparticle and LProd w/o iNGR were obtained 0.5, 4, and 12 h after intravenous injection. The arrows indicate tumor sites. All images were acquired under the same conditions (power density ≈ 200 mW cm^{-2}). (**E**) Fluorescent analysis of tumor sites in the LProd-, LProd w/o iNGR- and LPparticle-treated mice at 30 min, 2 h and 12 h after intraperitoneal injection (n = 3/group, mean ± s.d.). *P* values were calculated by *t*-test (*, $p < 0.05$; **, $p < 0.01$; ***, $p < 0.001$).

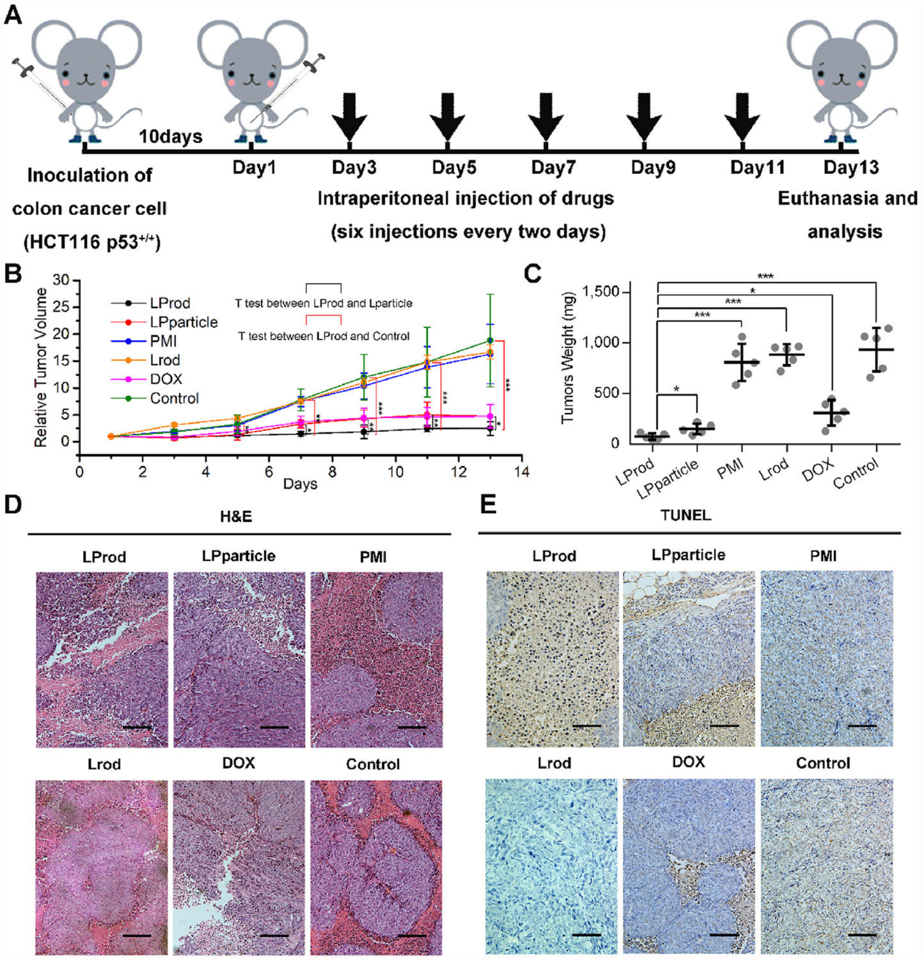

Fig. 7. *In vivo* antitumor activity of LProd.

(**A**) Schematic illustration of therapeutic process. Athymic nude mice (Balb/c) bearing HCT116 p53$^{+/+}$ were established and randomly divided into five groups (n = 5/group). Ten days following inoculation, mice were treated by the intraperitoneal injection every other day for 6 times with PBS, 1.5 mg/kg doxorubicin, 1.5 mg/kg PMI, 1.5 mg/kg Lrod, 1.5 mg/kg LProd or 1.5 mg/kg LPparticle, respectively. (**B**) Tumor growth curves in nude mice subcutaneously inoculated with 1 × 10^6 HCT116 cells into the right flank. The indicated treatments were administered every other day. Data are presented as mean ± s. e. (n = 5). (**C**) The weight of xenograft tumors from mice with the indicated treatments. Representative H&E (**D**) and TUNEL (**E**) stained images of xenograft tumors from mice with the indicated treatments (scale bar: 50 μm). *P* values were calculated by *t*-test (*, $p < 0.05$; **, $p < 0.01$; ***, $p < 0.001$).

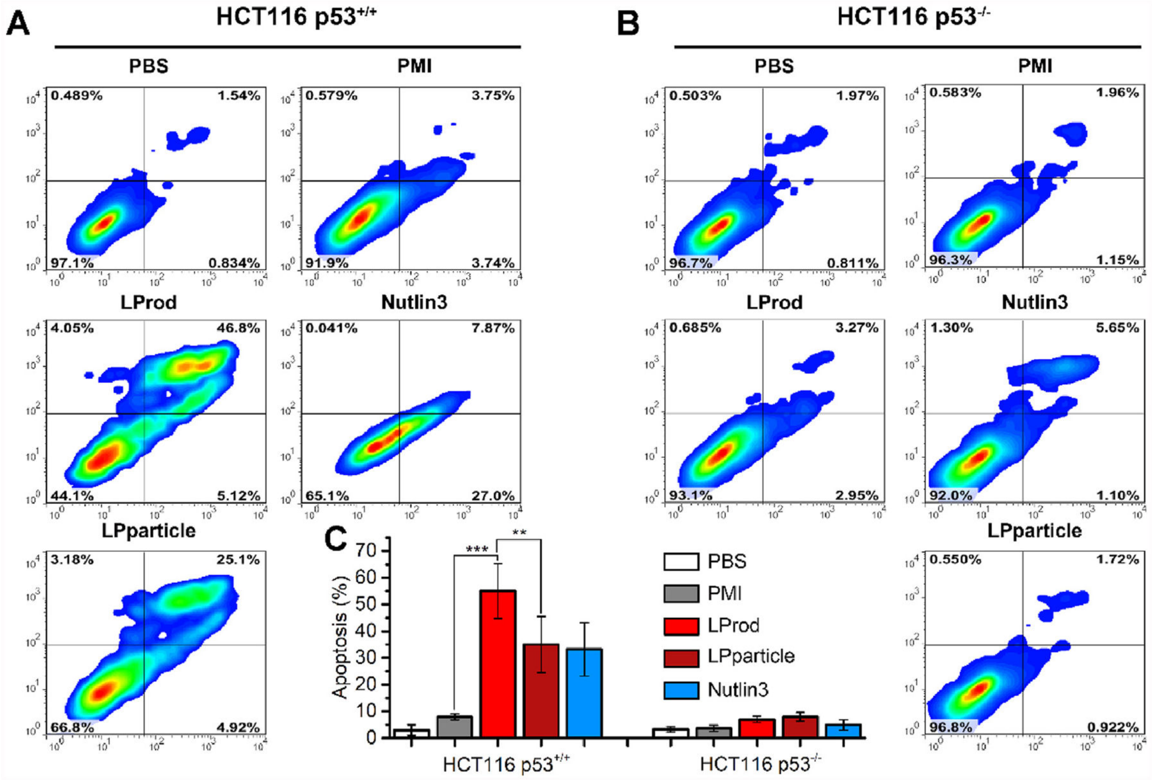

Fig. 8. LProd induces cancer cell apoptosis in a p53-dependent manner.

(**A**) The effect of LProd, PMI or Nutlin-3 on the apoptosis of HCT116 p53$^{+/+}$ cells. (**B**) The effect of LProd, PMI or Nutlin-3 on the apoptosis of HCT116 p53$^{-/-}$ cells. (**C**) Statistical analysis of cell apoptosis from three independent experiments in (**A**, **B**). The data were presented as mean ± s.d. *P* values were calculated by *t*-test (**, $p < 0.001$;***, $p < 0.001$).

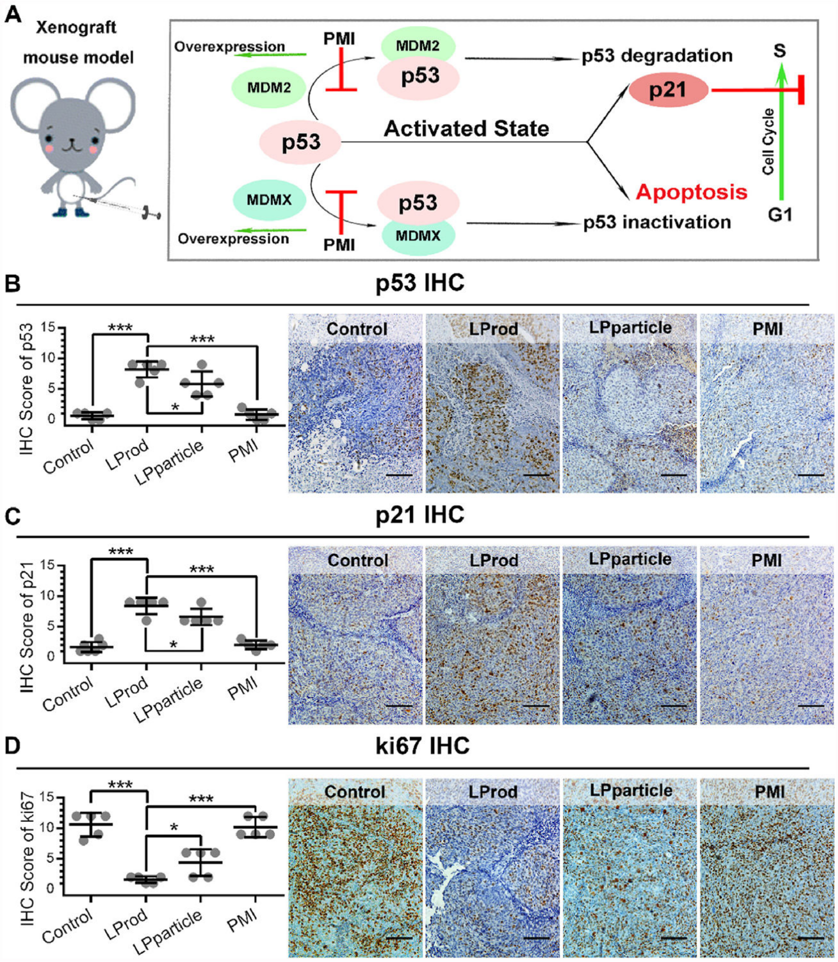

Fig. 9. The mechanism of LProd inhibiting tumor growth.

(**A**) Schematic diagram of antitumor efficacy of LProd by p53 restoration. (**B**–**D**) Representative immunohistochemistry (IHC) images and IHC score (**B** for p53, **C** for p21 and **D** for Ki67; scale bar: 50 μm) of tumor tissues from mice with the indicated treatments. *P* values were calculated by *t*-test (*, $p < 0.05$;**, $p < 0.01$;***, $p < 0.001$).

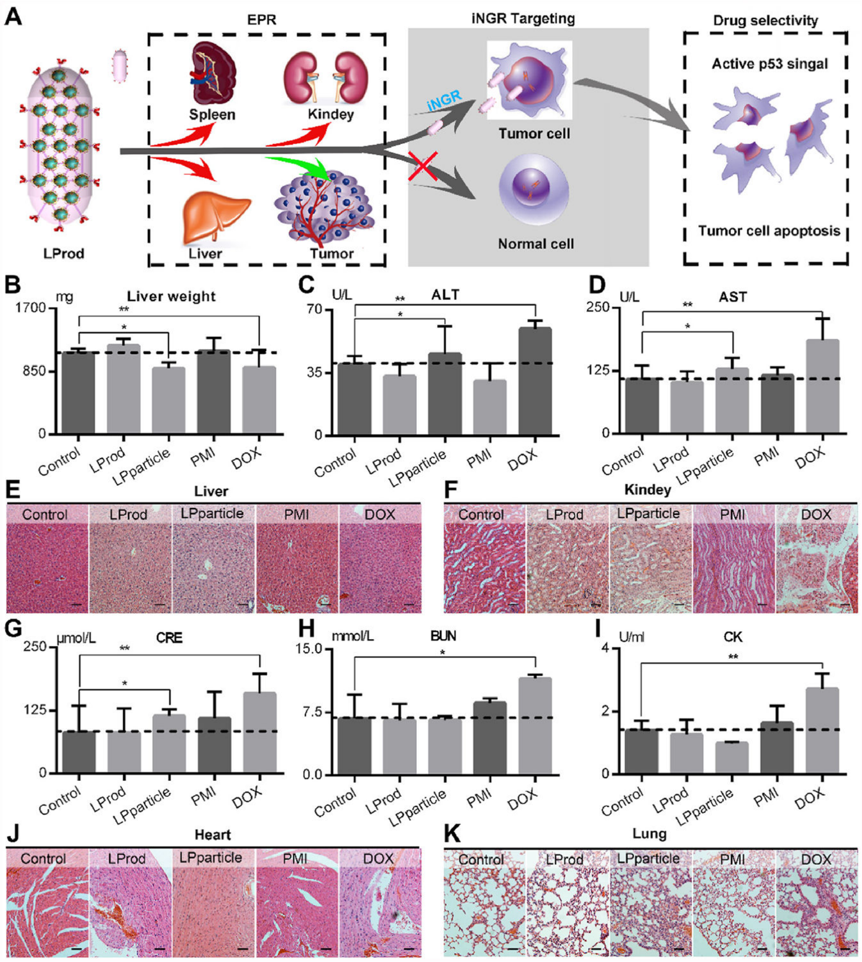

Fig. 10. *In vivo* safety evaluation of LProd.

(**A**) Schematic diagram for excellent biosafety of LProd attributed to its tumor-specific accumulation in the tumor sites other than organs. (**B**) Liver weight of mice with the indicated treatments. The activities of alanine transaminase (ALT, **C**) and aspartate aminotransferase (AST, **D**) related to liver function in mice with the indicated treatments. The representative histological H&E staining images of liver (**E**) and kidney (**F**) in mice with the indicated treatments (scale bar: 50 μm). Measurement of renal function indicators in mice with the indicated treatments (**G**: CRE = serum creatinine; **H**: BUN = blood urea nitrogen). (**I**) Creatine phosphokinase (CK) activity measured in the serum of mice with the indicated treatments, whose incensements are always accompanied by the cardiac trauma. The representative histological H&E staining images of heart (**J**) and lung (**K**) in mice with the indicated treatments (scale bar: 50 μm). P values were calculated by t-test (*, $p < 0.05$; **, $p < 0.01$).